Quaternary Science Reviews 156 (2017) 150–163

Contents lists available at ScienceDirect

Quaternary Science Reviews

journal homepage: www.elsevier.com/locate/quascirev

Authigenic Nd isotope record of North Pacific Intermediate Water formation and boundary exchange on the Bering Slope

Kwangchul Jang [a], Youngsook Huh [a, *], Yeongcheol Han [b]

[a] School of Earth and Environmental Sciences, Seoul National University, Seoul 08826, South Korea
[b] Division of Polar Paleoenvironment, Korea Polar Research Institute, Incheon 21990, South Korea

ARTICLE INFO

Article history:
Received 28 June 2016
Received in revised form
11 November 2016
Accepted 24 November 2016
Available online 19 December 2016

Keywords:
Neodymium
NPIW
Bering Sea
Authigenic
Brine
Ventilation
Seesaw

ABSTRACT

The Bering Sea is a potential location for the formation of the North Pacific Intermediate Water (NPIW), which drives the global ocean circulation as a counterpart to the North Atlantic Deep Water (NADW). To evaluate the NPIW-NADW seesaw hypothesis, we reconstructed the long-term variation of the bottom water Nd isotopic composition at site U1345 on the Bering Slope by extracting authigenic Fe-Mn oxyhydroxide from bulk sediments. We examined six different extractions in order to ensure that authentic seawater composition is recovered. For Bering Slope sediments whose typical carbonate content is less than 5% (average 2%), the most reliable results are obtained if the decarbonation step is omitted and a low reagent-to-sediment ratio is adopted.

The reconstructed authigenic ε_{Nd} record for the last 520 kyr exhibits large temporal variations depending on whether the NPIW formation or the boundary exchange process is dominant. Periods of radiogenic ε_{Nd} can be attributed to NPIW formation triggered by brine rejection, as evidenced by the difference in $\delta^{18}O$ of benthic foraminifera between sites ($\Delta\delta^{18}O_{bf}$), high % sea-ice related diatoms, and low abundance of *Bulimina aff. Exilis* (low-oxygen deep fauna). Diminished supply of unradiogenic Nd from boundary exchange seems to intensify these radiogenic peaks. On the other hand, the unradiogenic ε_{Nd} intervals can be attributed to stagnant bottom water conditions, as can be deduced from the $\Delta\delta^{18}O_{bf}$ values, low % sea-ice related diatoms, abundant *B. aff. Exilis*, and laminations. When there is no NPIW formation, the continental margin sediments are exposed to boundary exchange for a longer period of time, leading to release of unradiogenic Nd. The mid-MIS 6 and mid-MIS 5 are exceptions in that NPIW formation occurred yet the ε_{Nd} compositions are unradiogenic. NPIW formation and cold climate (closed Bering Strait) are not always correlated. Comparison against ε_{Nd} records of the South Atlantic suggests only an ambiguous NPIW-NADW seesaw for the last 200 kyr.

© 2016 Elsevier Ltd. All rights reserved.

1. Introduction

The formation of intermediate and deep water plays an important role in the global climate system as a driving force of global ocean circulation and as a regulator of greenhouse gases such as carbon dioxide (CO_2) (Biastoch et al., 2008; Häkkinen and Rhines, 2004; Stouffer et al., 2006). The North Atlantic Deep Water (NADW) is one such example, and past variations in its strength are well documented, e.g., the reduction in NADW formation and related climate change during the Younger Dryas (YD) and the Heinrich events (HE) (Sarnthein et al., 1994; Seidov and Maslin, 1999). There is no deep-water formation in the North Pacific at present due to the low surface water salinity. Intermediate water forms in the Okhotsk Sea through brine rejection, but the magnitude is relatively small compared to the NADW (Shcherbina et al., 2003; Talley, 1991; Yasuda, 1997).

Recent research shows that the formation of the North Pacific Intermediate Water (NPIW) was stronger during glacial periods and that the Bering Sea was a probable location (Horikawa et al., 2010; Ohkushi et al., 2003; Rella et al., 2012). For example, Ohkushi et al. (2003) propose that NPIW formed in the Bering Sea during the Last Glacial Maximum (LGM), based on the spatial distribution pattern of radiolarian species *Cycladophora davisiana*, which lives in a cold and well-oxygenated habitat such as the present NPIW environment. Supporting evidence comes from the $\delta^{18}O$ of benthic foraminifera ($\delta^{18}O_{bf}$) on the Bering Slope (MR06-04-23, 60°09.52′N,

* Corresponding author.
E-mail address: yhuh@snu.ac.kr (Y. Huh).

http://dx.doi.org/10.1016/j.quascirev.2016.11.032
0277-3791/© 2016 Elsevier Ltd. All rights reserved.

179°27.82′W; 1002 m water depth) (Rella et al., 2012) (Fig. 1). There is a positive $\delta^{18}O_{bf}$ excursion during the LGM that cannot be interpreted by an increase in global ice volume alone but requires the intrusion of colder and/or more saline water to the site (Rella et al., 2012). Rella et al. (2012) suggest that NPIW formed during other cold periods as well, such as HE 1 and 4 and YD, based on the positive $\delta^{18}O_{bf}$ gradient between the Bering Slope and the Okhotsk Sea. Horikawa et al. (2010) use a different proxy to arrive at similar conclusions. The neodymium (Nd) isotopic composition of the intermediate water on the Bowers Ridge in the Bering Sea (BOW-8A, 54°47′N, 176°55′E, 884 m water depth) over ~150 kyr shows radiogenic peaks during glacial periods, which they interpret as periods of NPIW formation (Horikawa et al., 2010) (Figs. 1 and 2).

The premise of the NPIW-NADW seesaw hypothesis is that when NADW formation is diminished, NPIW formation regulates the global climate system by driving global ocean circulation and by distributing heat from equator to pole (Okazaki et al., 2010). Accordingly, periods of strong NPIW should correlate with those of weak NADW. Several model simulations suggest a seesaw relationship between NPIW/NPDW and NADW (Hu et al., 2012a; Okazaki et al., 2010; Saenko et al., 2004), but proxy studies are controversial. One proxy, the ^{14}C ventilation age, is determined by the difference in ^{14}C age between coexisting benthic and planktonic foraminifera. A low ^{14}C ventilation age indicates downwelling or upwelling. Okazaki et al. (2010) report an anti-phase relationship in ^{14}C ventilation ages between NPIW/NPDW (1000–2700 m water depth) and NADW during HE 1. Max et al. (2014) also show an anti-phase relationship between NPIW (700–1750 m water depth) and NADW during HE 1 and YD, but they argue against the seesaw with regard to NPDW (2100–2700 m water depth). An in-phase correlation between NPDW (2300 m water depth) and NADW during HE 1 is documented by Sarnthein et al. (2013). Another proxy is the $\delta^{13}C_{bf}$ difference between two sites ($\Delta\delta^{13}C_{bf}$), which can be used as a proxy for NPIW or NADW formation (Knudson and Ravelo, 2015). A cross-spectral analysis of $\Delta\delta^{13}C_{bf}$ over 1.2 Myr does not exhibit an anti-correlation between NPIW (818 m) and NADW, and it challenges the orbital-scale "seesaw" behavior (Knudson and Ravelo, 2015). This disagreement among proxies may be due to several factors. First, the uncertainty in the carbon reservoir age leads the authors to propose incompatible NPIW/NPDW behavior. For example, Okazaki et al. (2010) applied a smaller reservoir age ($\Delta R = 100$ yr) than Max et al. (2014) ($\Delta R = 900$ yr), which led them to propose NPDW formation during the cold HE 1 (Okazaki et al., 2010) and during the warm Bølling/Allerød (Max et al., 2014). Second, water mass-dependent variation in $\delta^{13}C_{bf}$ can be smoothed out by biological productivity, air-sea gas exchange and/or calcite preservation. Third, the seesaw behavior may be episodic, e.g., only

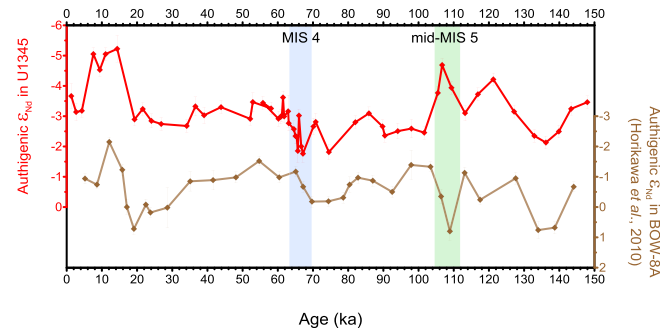

Fig. 2. Comparison of ε_{Nd} values between sites U1345 (red) and BOW-8A (brown). The persistent offset (2–3 ε_{Nd}) between the two sites is likely due to unradiogenic input to site U1345 from boundary exchange processes. The gap decreases during MIS 4 (blue bar) and increases during mid-MIS 5 (green bar) (see Sections 4.4.1 and 4.4.2). (For interpretation of the references to colour in this figure legend, the reader is referred to the web version of this article.)

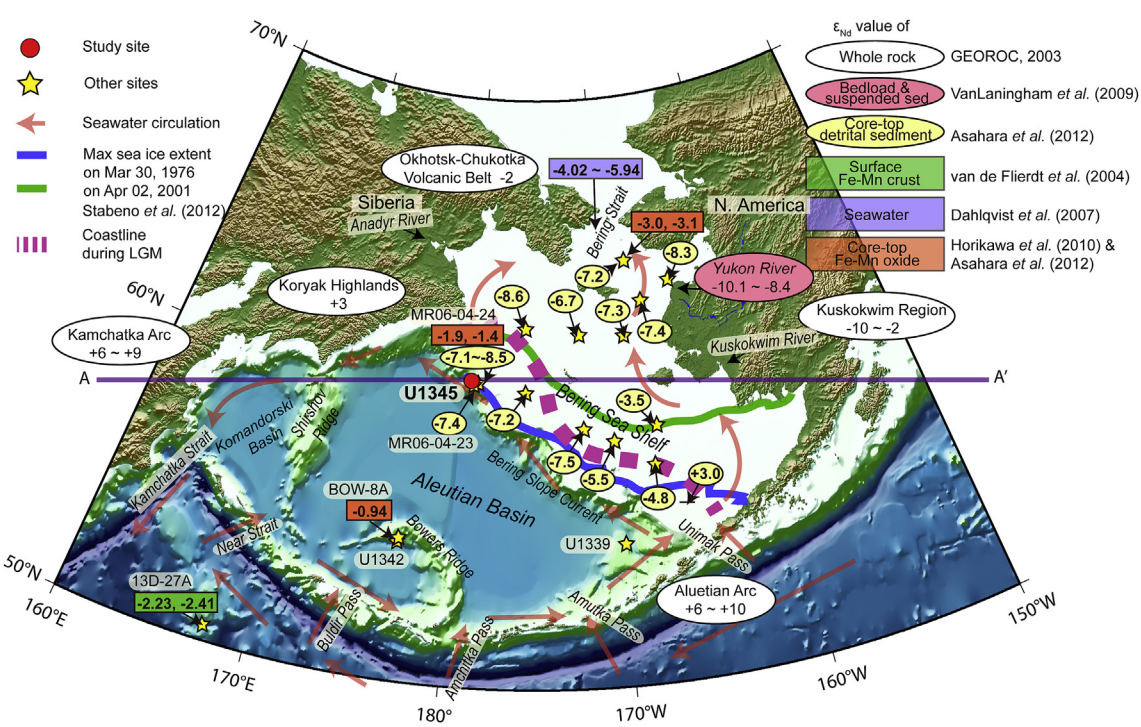

Fig. 1. The Nd isotopic compositions (ε_{Nd}) near site U1345 (red circle) in the Bering Sea. The ε_{Nd} values are given in ellipses and rectangles. Red arrows indicate the direction of ocean circulation. Maximum sea ice extent in 1976 (cold winter) and in 2001 (warm winter) is shown with blue and green lines, respectively (Stabeno et al., 2012). Purple dashed line indicates the coastline at the LGM. A schematic illustration of the AA′ cross section is shown in Fig. 6. (For interpretation of the references to colour in this figure legend, the reader is referred to the web version of this article.)

when freshwater discharge interrupts NADW formation like during HE 1. Therefore, a sufficient data-set covering multiple glacial-interglacial cycles with different proxies is necessary.

The Nd isotope ratio is a quasi-conservative water mass tracer (Frank et al., 2002; Rutberg et al., 2000). ^{143}Nd is the daughter isotope of ^{147}Sm, and the ^{143}Nd/^{144}Nd ratio in rocks is primarily determined by their Sm/Nd ratio and age. The Nd isotopic composition is reported as ε_{Nd}, where $\varepsilon_{Nd} = [(^{143}Nd/^{144}Nd)_{sample}/(^{143}Nd/^{144}Nd)_{CHUR} - 1] \times 10^4$ and $(^{143}Nd/^{144}Nd)_{CHUR}$ is 0.512638 (Jacobsen and Wasserburg, 1980). The ε_{Nd} values of local rocks influence those of adjacent sea water, as indicated by the similarity of ε_{Nd} values between the ocean and the surrounding continents (e.g., Arsouze et al., 2007; Lacan and Jeandel, 2005). For example, the ε_{Nd} values of the Pacific Ocean (ε_{Nd} ~0 to +4) surrounded by young volcanic rocks are more radiogenic than the Atlantic Ocean (ε_{Nd} ~ -13) surrounded by old continental rocks, and ε_{Nd} in the Circumpolar Deep Water (CDW) is intermediate, reflecting mixing of the two water masses (ε_{Nd} ~ −9 to −6) (data from Albarède and Goldstein, 1992 and references therein; Albarède et al., 1997). This pattern attests to the residence time of Nd shorter than the ocean mixing time (Tachikawa et al., 1999) and to the utility of Nd isotopes as a quasi-conservative water mass tracer. The good correlation between ε_{Nd} and the salinity of seawater supports the effectiveness of this proxy (von Blanckenburg, 1999).

The bottom water ε_{Nd} is regulated by external and internal sources. External Nd sources are lateral advection (e.g. mixing between NADW and CDW; Rutberg et al., 2000) and vertical mixing (e.g. NADW formation) of water masses, and internal sources are boundary exchange (e.g., Arsouze et al., 2007) and pore water diffusion (e.g., Abbott et al., 2015). In the Atlantic, water circulation at present is relatively fast and vigorous due to NADW formation, and the effectiveness of internal sources is reduced. Thus, ε_{Nd} can be used as a water mass tracer (Siddall et al., 2008). In the Pacific, water circulation is more sluggish (Siddall et al., 2008), and internal sources need to be taken into account. Indeed, ε_{Nd} change in Pacific deep waters at present cannot be interpreted solely by water mass mixing (Abbott et al., 2016). Likewise, negligible NPIW formation in the Bering Sea at present (Warner and Roden, 1995) implies that bottom water ε_{Nd} is mainly determined by internal sources. However, stronger NPIW formation in the Bering Sea in the past may switch the main Nd source from internal to the external, and provide a perspective on the interplay between external and internal sources controlling bottom water ε_{Nd}.

We use the authigenic Fe-Mn oxyhydroxide coating of marine sediments as an archive of seawater Nd isotopic composition. Dissolved Nd is incorporated into the authigenic coating when it precipitates. Because this Fe-Mn oxyhydroxide coating is extracted from bulk sediments using chemical reagents, the dissolution of labile non-authigenic material (e.g., volcanic material) during the leaching process may bias the Nd isotope ratios (Roberts et al., 2010). The potential incorporation of non-authigenic components is tested by comparing the ε_{Nd} of bulk sediment leachate with that of biogenic material such as foraminifera or coral reef (Martin and Scher, 2004; Roberts et al., 2010; van de Flierdt et al., 2010). In these tests, elemental concentration criteria (e.g., Al/Nd and REE pattern) are used to verify the authenticity of the leachates (Blaser et al., 2016; Martin et al., 2010; Wilson et al., 2013).

Here, we provide orbital-scale variations in NPIW at 1008 m using the isotope ratio of seawater-originated Nd on the Bering Slope, the most probable location of NPIW formation within the Bering Sea, as inferred from the distribution pattern of the *C. davisiana* during the LGM (Ohkushi et al., 2003). To acquire an authentic seawater signal in the Bering Sea, we first compare the Nd isotope ratio and elemental concentrations derived from three conventional extraction methods and determine the most appropriate method for Bering Slope sediments. With the Nd isotope record, we can constrain whether NPIW formation or boundary exchange processes control the bottom water ε_{Nd} on the Bering Slope. Then, we examine the relationships between NPIW formation and cold climate and between NPIW and NADW.

2. Materials

2.1. Sampling location

Sediment core samples are from site U1345 (60°9′N, 179°28′W; 1008 m water depth), drilled on the western part of the Bering Slope during the Integrated Ocean Drilling Program Expedition 323 (Fig. 1). Site U1345 is influenced by tidal mixing and the Bering Slope Current (BSC) that flows westward along the continental shelf. This water circulation contributes to the high nutrient concentration and high biological productivity at this site (Springer et al., 1996), and the high sedimentation rate (>30 cm/kyr) is favorable for obtaining a high-resolution record. This site is near the present-day maximum sea ice extent (Katsuki and Takahashi, 2005) and is located in the modern oxygen minimum zone (OMZ) (Takahashi et al., 2011).

From a geological perspective, potential Nd sources to this site are the unradiogenic inflow from North America, e.g., the particulate matter carried by the Yukon River (ε_{Nd} ~ −10.1 to −8.4) (data from VanLaningham et al., 2009), and the radiogenic inflows from the Aleutian Arc and the Kamchatka Arc, which are mainly composed of volcanic rocks (ε_{Nd} ~+6 to +10 and + 6 to +9, respectively) (data from GEOROC, 2003) (Fig. 1). The Anadyr River in Siberia (ε_{Nd} ~ −2 to +3) can be a possible source in case of low sea level (see Section 4.4.1) (Fig. 1). The inflow from Kamchatka seems to be relatively small in terms of present-day water circulation.

2.2. Core description

Among the five cores (Holes A to E) at site U1345, we used Hole A (60°9.19′N, 179°28.20′W; 1007.3 m water depth; core length 147.43 mbsf) as the main core to reconstruct Nd isotope ratios and Hole C (60°9.21′N, 179°28.22′W; 1008.8 m water depth; core length 148.53 mbsf) and D (60°9.22′N, 179°28.23′W; 1008.3 m water depth; core length 150.51 mbsf) as sub cores to complement its continuity. The stratigraphic correlation between them was based on the Whole-Round Multisensor Logger magnetic susceptibility (MS), gamma ray attenuation (GRA) bulk density, natural gamma radiation (NGR) and color reflectance parameter b* (Expedition 323 Scientists, 2011), and the revised depth scale is expressed in CCSF-A (m).

The sediments are mainly siliciclastic with a varying amount of diatoms and typically <10% foraminifera and calcareous nannofossils. Laminations usually appear in diatom-rich layers with lower MS, GRA bulk density and NGR counts and higher b* values. Shipboard observations report a few ash layers in U1345A (0–4.39 CCSF-A (m)), U1345C (0.09–6.05 and 112.62–122.70 CCSF-A (m)), and U1345D (135.76–145.70 CCSF-A (m)), but ash layers are probably more widespread (Expedition 323 Scientists, 2011).

We applied the age model constructed by Cook et al. (2016). Eleven age control points were assigned based on the correlation of the oxygen isotope ratio of benthic foraminifera with the global LR04 stack. The age of U1345 extends to ~520 ka, and the average sedimentation rate is ~31.3 cm kyr^{-1} without a significant difference between glacial (20.7–45.1 cm kyr^{-1}) and interglacial periods (19.7–46.4 cm kyr^{-1}).

3. Method

3.1. Separation of authigenic and detrital fractions

3.1.1. Authigenic Fe-Mn oxyhydroxide fraction

The authigenic Fe-Mn oxyhydroxide fraction records past seawater composition and is therefore our main interest. During the extraction process, it is very important to avoid the dissolution of non-authigenic material. The dissolution of terrigenous components mainly depends on lithology; therefore, the chemical protocol needs to be adjusted to the specific site (Wilson et al., 2013). To determine the most suitable extraction method for the Bering Slope sediments, we first carried out a test on four sediment samples representing opposing climate regimes: Holocene and marine isotope stage (MIS) 5.5 warm periods and LGM and MIS 4 cold periods. We tested three different extraction methods on these four samples.

The first method is modified from Rutberg et al. (2000) (hereafter, *Rutberg Authigenic*), and it subjects de-carbonated samples to 0.02 M hydroxylamine hydrochloride (HH) in 25% buffered acetic acid for 3 h (Table 1). The reagent-to-sediment volume ratio is approximately 10. The second method is based on Wilson et al. (2013) (hereafter, *Wilson Authigenic*). There is no decarbonation step, the leaching time is shorter (1 h), and the reagent-to-sediment volume ratio is lower (~1). The third method (hereafter, *Blaser Authigenic*) is similar to *Wilson Authigenic*, but the reducing reagent is different (0.005 M HH in 1.5% buffered acetic acid with 0.003 M Na-EDTA), and the reagent-to-sediment volume ratio is higher (>30) (Blaser et al., 2016).

3.1.2. Carbonate fraction and second authigenic fraction

These two fractions are used to constrain the range of seawater ε_{Nd}. The best way to ensure the authenticity of the authigenic ε_{Nd} value is to compare it with the coating on biogenic material such as foraminifera (Roberts et al., 2010). However, the siliceous biogenic environment on the Bering Slope does not provide enough calcareous biogenic material for Nd isotope analysis. Thus, we resorted to the carbonate fraction and the second authigenic fraction (hereafter, *Second Authigenic*).

The carbonate fraction is extracted with 1 M buffered acetic acid for 12 h (Table 1). The lack of detrital carbonate input into the Bering Sea assures us that the carbonate fraction is mainly composed of authigenic carbonate (Hein et al., 1979) and that it essentially reflects the sea water composition. Indeed, the carbonate fraction has been used as an archive for Nd isotopic composition of the bottom water in the Bering Sea (Akagi et al., 2014) and the Arctic Ocean (Akagi et al., 2014; Haley and Polyak, 2013), although different concentrations of reagent and leaching times were used for the extraction (40% acetic acid for 10 min and 1 M buffered acetic acid for 30 min, respectively).

The *Second Authigenic* is obtained by submitting the remaining sediment after the *Rutberg Authigenic* extraction to a second round of Fe-Mn oxyhydroxide extraction, this time for 24 h. The possibility of dissolution of labile terrigenous component increases with the leaching time; therefore, the *Second Authigenic* is a contaminable fraction. Consequently, the ε_{Nd} values of the carbonate fraction and the *Second Authigenic* can restrict the range in ε_{Nd} value of authigenic Fe-Mn oxyhydroxide.

3.1.3. Detrital fraction

After complete separation of the authigenic fraction, alkaline fusion is carried out on the residue (Bayon et al., 2009). We mix 0.1 g residue with 1.2 g Na_2O_2 (>95%, small beads, ACS grade, Sigma-Aldrich) and 0.6 g NaOH (>98.0%, pellet, ACS grade, Sigma-Aldrich) in a glassy carbon beaker (SIGRADUR, HTW). This mixture is fused at 650 °C for 15 min and re-dissolved in deionized water after slight cooling at room temperature. The melt is transferred into a Teflon beaker and placed on the hotplate at 130 °C for complete co-precipitation. After centrifugation, the precipitate is used for detrital Nd isotope analysis. The 48 samples and reference materials (JB-2 and BHVO-1) were treated with the same alkaline fusion procedure (see Section 3.2.3).

3.2. Purification and instrumental analysis

3.2.1. Elemental concentrations of the different fractions

We measured the concentrations of select elements (Al, Fe, Mn, Sr, and REEs) in the five non-detrital fractions of the LGM and MIS 5.5 sediment samples. We used an inductively coupled plasma-sector field mass spectrometer (ICP-SFMS, Element 2, Thermo Scientific) at the National Center for Inter-University Research Facilities of Seoul National University. The oxide production rate was reduced using a desolvation nebulizer system (Aridus II, Cetac) ($^{135}Ba^{16}O/^{135}Ba$ ~0.01%). The external reproducibility was better than 5%. The average elemental concentrations for the river water reference material SLRS-4 agreed within literature values (Heimburger et al., 2013; Soyol-Erdene and Huh, 2013), except for Lu, which we do not use here.

3.2.2. Column separation

Two column separation steps were carried out using TRU resin (50–100 μm, Eichrom) and Ln resin (50–100 μm, Eichrom), following methods modified from Míková and Denková (2007) and Pin and Zalduegui (1997). The authigenic fractions were dissolved in 2 M HNO_3 and loaded onto the TRU resin. After eluting the fraction containing HREEs with 2 M HNO_3, LREEs were retrieved with 0.05 M HCl. The LREE fraction was loaded onto the Ln resin. With 0.15 M HCl, La, Ce, and Pr were eluted and Nd was retrieved.

3.2.3. Nd isotope composition

Nd isotope ratios were measured using the thermal ionization mass spectrometer (TIMS, Triton, Thermo Scientific) at the Korea Polar Research Institute and the multicollector inductively coupled plasma mass spectrometer (MC-ICP-MS, Neptune, Thermo

Table 1
Three different extraction methods for the authigenic Fe-Mn oxyhydroxide fraction.

Fraction	Rutberg et al. (2000)		Wilson et al. (2013)		Blaser et al. (2016)	
	Reagent	Time (hr)	Reagent	Time (hr)	Reagent	Time (hr)
Carbonate	1 M Buffered acetic acid	12	–	–	–	–
Fe-Mn oxide	0.02 M HH[a] in 25% buffered acetic acid	3	0.02 M HH in 25% buffered acetic acid	1	0.005 M HH in 1.5% buffered acetic acid with 0.003 M Na-EDTA	1
Reagent/Sample(v/v)	~10		~1		>30	

[a] HH: hydroxylamine hydrochloride.

Scientific) at the Korea Basic Science Institute. We used $^{147}Sm/^{146}Nd$ for interference correction and $^{146}Nd/^{144}Nd$ for mass fractionation correction by normalizing to 0.7219. The $^{143}Nd/^{144}Nd$ ratios and external reproducibilities of the JNdi-1 standard were 0.512098 ± 0.000011 (2σ, n = 30) for TIMS, 0.512101 ± 0.000017 (2σ, n = 8) for the first MC-ICP-MS analysis, and 0.512103 ± 0.000015 (2σ, n = 11) for the second MC-ICP-MS analysis. The $^{143}Nd/^{144}Nd$ ratios of JB-2 and BHVO-1 were 0.513095 ± 0.000011 and 0.512983 ± 0.000010, respectively, which are consistent with literature values (Weis et al., 2005; Yang et al., 2009 and references therein). The external reproducibility on the standard is reported as the final uncertainty unless it is smaller than the internal standard error of the samples.

3.3. Reconstruction of the sea water Nd isotopic composition

We extracted *Wilson Authigenic* from 102 sediment samples including four duplicates and *Rutberg Authigenic* from 113 sediment samples including 19 duplicates. Ninety-seven *Wilson Authigenic* and one *Rutberg Authigenic* were used for reconstruction of the past oceanic neodymium isotopic composition (see Section 4.1). Included were five samples from the four ash layers (see Section 2.2). The average depth and age interval between samples are ~1.7 CCSF-A (m) and 5.3 kyr, respectively. Each sample covers 10–100 yr.

4. Results and discussion

4.1. Test for the most suitable extraction method

4.1.1. ε_{Nd} and elemental composition results

The Nd isotopic composition of the six different fractions of the four test samples is shown in Fig. 3A, B, K and L. When the extraction test was repeated, the ε_{Nd} of each fraction was reproduced within uncertainty (0.2–0.5 ε_{Nd}) (Fig. 3B). The detrital fraction had different ε_{Nd} in the duplicate extractions, probably due to sediment heterogeneity. Of the six different fractions, the detrital fraction has the lowest ε_{Nd} value. Among the non-detrital fractions, the carbonate fraction and *Wilson Authigenic* have lower ε_{Nd} values, and *Blaser Authigenic* and *Second Authigenic* have higher values. *Rutberg Authigenic* displays similar to slightly more radiogenic ε_{Nd} values than *Wilson Authigenic*.

The ε_{Nd} difference between fractions is prominent in samples #1 (MIS 5.5) and #4 (MIS 4): the carbonate fraction and *Wilson Authigenic* are distinctly less radiogenic than the other authigenic fractions. On the other hand, in samples #2 (LGM) and #3 (Holocene), the ε_{Nd} values of *Wilson Authigenic* and *Rutberg Authigenic* are similar. This sample-dependent ε_{Nd} variation among the different authigenic fractions can result from lithology. Volcanic material is most prone to inducing a radiogenic ε_{Nd} bias, and hence, a higher volcanic content is predicted for samples #1 and #4. The carbonate content is also important because its lability delays dissolution of the volcanic component. The decarbonation step for *Rutberg Authigenic* and *Second Authigenic* and the faster carbonate removal by EDTA for *Blaser Authigenic* may accelerate Nd isotope exchange with the volcanic component and introduce a radiogenic ε_{Nd} bias.

Unlike ε_{Nd}, elemental concentrations cannot independently distinguish whether terrigenous components are leached. We do not observe any significant correlation between ε_{Nd} and elemental concentrations. The Nd concentration is high in the *Blaser Authigenic* of both samples #1 and #2 (Fig. 3A and B), and judging from the radiogenic ε_{Nd} values, there is dissolution of volcanic material. However, the other fractions display low Nd concentrations with varying ε_{Nd} values. Aluminum, an element abundant in clay minerals, exhibits a similar trend as Nd (Fig. 3C and D).

The Al/Nd ratio has been used as an indicator for dissolution of the detrital fraction (Gutjahr et al., 2007). For sample #1, there is a broad inverse relationship between Al/Nd and ε_{Nd}, with the lowest Al/Nd in *Second Authigenic* (Fig. 3C). For sample #2, there is no correlation between Al/Nd and ε_{Nd}, with relatively high Al/Nd in *Second Authigenic* (Fig. 3D). This irregular relationship between Al/Nd and ε_{Nd} requires further examination for the Al/Nd parameter (Martin et al., 2010; Wilson et al., 2013). Iron and manganese, main components of Fe-Mn oxyhydroxide, are also highest in *Blaser Authigenic* (Fig. 3E and F). We observe a roughly increasing trend of Fe concentration with increasing ε_{Nd} only in sample #2. The concentration of Sr is highest in *Blaser Authigenic*, which is consistent with the other elemental concentrations (Fig. 3G and H). It is lowest in *Rutberg Authigenic* and *Second Authigenic*, which can be attributed to the removal of Sr in the decarbonation step.

We also examined the REE pattern to evaluate the seawater origin of leachate ε_{Nd} (Martin et al., 2010). The MREE/MREE* and HREE/LREE ratios quantify the extent of the MREE bulge and HREE enrichment, respectively. *Wilson Authigenic* displays the highest MREE/MREE* and HREE/LREE ratios and the *Second Authigenic* the lowest (Fig. 3I and J). Most fractions show MREE bulge patterns (MREE/MREE* > 1) and moderate to enriched HREE (HREE/LREE > 1), which is consistent with typical hydrogenous Fe-Mn oxyhydroxides, fish teeth and Fe-Mn nodules (Axelsson et al., 2002; Bayon et al., 2002; Gutjahr et al., 2007; Jauhari and Pattan, 2000; Martin et al., 2010; Sherrell et al., 1999). *Second Authigenic* is the only exception, with an HREE/LREE ratio lower than 1. We do not detect a specific relationship between the REE pattern and ε_{Nd} in our restricted data set.

We compared the Nd isotopic compositions of *Wilson Authigenic* and *Rutberg Authigenic* (n = 113, including duplicates). They are mostly consistent with each other within uncertainty (n = 94), but 19 data points—18 *Rutberg Authigenic* and one *Wilson Authigenic*—are more radiogenic than the 1:1 line (Fig. 4). All duplicates of *Wilson Authigenic* have consistent ε_{Nd} values, but five of the 19 duplicates for *Rutberg Authigenic* display inconsistent ε_{Nd} values and are also more radiogenic than the corresponding *Wilson Authigenic*. Among the five ash layer samples mentioned in Section 2.2, *Rutberg Authigenic* is more radiogenic than *Wilson Authigenic* in three samples, indicating the vulnerability of *Rutberg Authigenic* to contamination from volcanic material (Fig. 4, red symbols).

4.1.2. Leaching protocol for Bering Sea sediments

We propose that the *Wilson* method is the most appropriate to extract an authentic seawater signal from the Bering Slope sediments. This is based on a comparable ε_{Nd} of *Wilson Authigenic* and carbonate fractions (Fig. 3), a lower ε_{Nd} of *Wilson Authigenic* compared to other authigenic fractions (Fig. 3), and the general consistency between the ε_{Nd} of *Wilson Authigenic* and *Rutberg Authigenic* and a more radiogenic *Rutberg Authigenic* where there are inconsistencies between the two (Fig. 4).

The comparable ε_{Nd} of *Wilson Authigenic* and carbonate fractions supports that *Wilson Authigenic* records a seawater-originated Nd isotopic signal. We consider the carbonate fraction to be free from contamination by terrigenous components, as this mildest leaching treatment reduces the risk of dissolution of labile terrigenous material. The carbonates at site U1345 are dominantly authigenic and biogenic (Expedition 323 Scientists, 2011), which rules out the possibility of an ε_{Nd} shift by detrital carbonate. The influence of diagenetic carbonate overgrowth is probably minimal. The carbonate fraction displays an MREE bulge pattern (Fig. 3I and J) that is distinct from the low MREE/MREE* and very high HREE/LREE of the neighboring pore waters (Soyol-Erdene and Huh, 2013). For these reasons, the carbonate fraction would essentially reflect a seawater Nd isotopic composition, as would *Wilson Authigenic*.

The lower ε_{Nd} of *Wilson Authigenic* compared to other authigenic

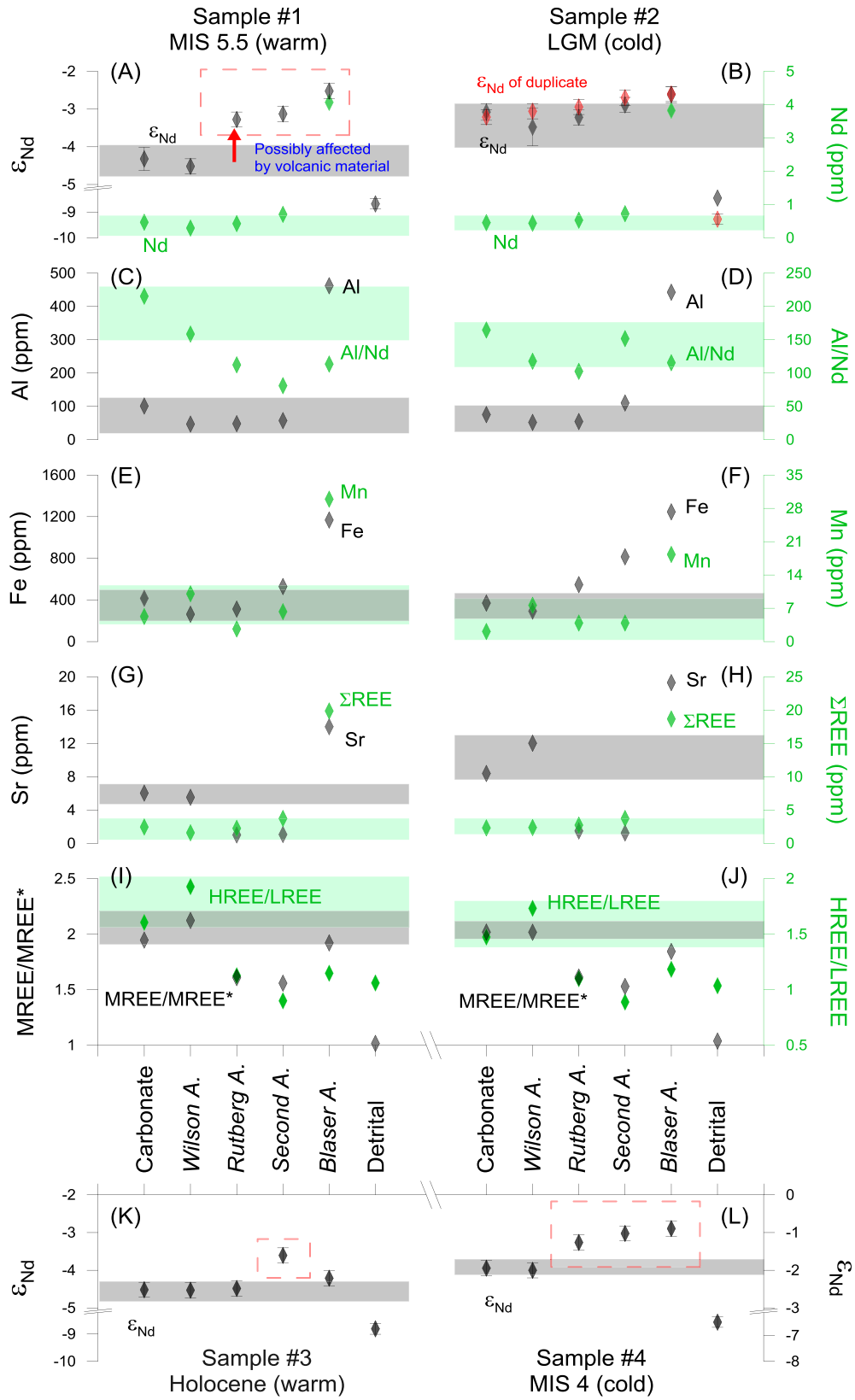

Fig. 3. TIMS (ε_{Nd}) and ICP-SFMS (Nd, Al, Al/Nd, Fe, Mn, Sr, ΣREE, MREE/MREE* and HREE/LREE) results for six different fractions (carbonate; authigenic Fe-Mn oxide of Wilson, Rutberg, and Blaser methods; *Second Authigenic*; and detrital) for the LGM and MIS 5.5 sediment samples (A to J). For the Holocene and MIS 4 (K and L) samples, only ε_{Nd} was analyzed. MREE/MREE* = $(Gd_n + Tb_n + Dy_n)/[\{(Tm_n + Yb_n \times 2) + (La_n + Pr_n + Nd_n)\}/2]$, HREE/LREE = $(Tm_n + Yb_n \times 2)/(La_n + Pr_n + Nd_n)$ (subscript n denotes PAAS normalized concentration) (after Martin et al., 2010 but Lu_n replaced by Yb_n). Dashed red boxes mark radiogenic ε_{Nd} results, possibly affected by labile terrigenous components. Gray and green shaded areas mark the data range of carbonate and *Wilson Authigenic* fractions, which we take to be the true authigenic fraction. Elemental concentrations are not powerful criteria to determine the data reliability of authigenic ε_{Nd}. (For interpretation of the references to colour in this figure legend, the reader is referred to the web version of this article.)

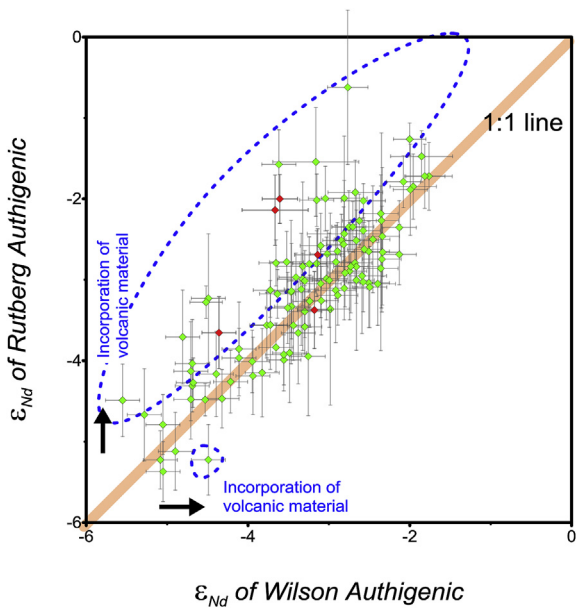

Fig. 4. Comparison of Rutberg and Wilson methods (n = 113, including 19 duplicates). Dashed blue circles mark contaminated ε_{Nd} values, and the red symbols indicate the samples in ash layers (see Section 2.2). (For interpretation of the references to colour in this figure legend, the reader is referred to the web version of this article.)

fractions also indicates an authentic seawater signal. The stronger extraction of *Second Authigenic* than *Rutberg Authigenic* releases radiogenic volcanic material that is more reactive than the remaining detrital fraction (Fig. 3) (Wilson et al., 2013). Therefore, the lower ε_{Nd} values represent a reduced influence from terrigenous sources.

The general similarity of the ε_{Nd} between *Wilson Authigenic* and *Rutberg Authigenic* suggests data validity. Radiogenic exceptions are mainly observed in *Rutberg Authigenic* (Fig. 4), suggesting that the stronger extraction of *Rutberg Authigenic* may release some terrigenous components. There was only one occasion of radiogenic bias for *Wilson Authigenic*, and therefore, we consider the treatment method of *Wilson Authigenic* to be stable. We replaced the radiogenic outlier of *Wilson Authigenic* with the corresponding *Rutberg Authigenic* (Fig. 5B, blue symbol).

We cannot rely on elemental concentrations to detect unintended incorporation of terrigenous material into sediment leachate (Fig. 3). All elemental concentrations and the Al/Nd ratio are independent of ε_{Nd} variation. The Al/Nd ratio is highest in the carbonate and not the detrital fraction, suggesting that re-adsorption of REEs during extraction may modify this ratio (Wilson et al., 2013). Therefore, careful use of elemental criteria is necessary.

We suggest that *Wilson Authigenic* is a reliable fraction for recording seawater-origin Nd isotopic compositions in the Bering Slope, although we cannot provide unambiguous proof due to the lack of ε_{Nd} data for foraminifera and the water column. *Wilson Authigenic* is appropriate especially for sediments whose detrital carbonate content is negligible. Because carbonate is more labile than volcanic material, the presence of carbonate delays the Nd isotopic exchange of leachate with volcanic material (Wilson et al., 2013). Low chemical reagent-to-sediment ratios provide sufficient available surface area for Nd re-adsorption, slowing down exchange with non-authigenic radiogenic components (Wilson et al., 2013). EDTA has a similar effect because it forms complexes with REEs and reduces re-adsorption (Gutjahr et al., 2007). Considering that *Rutberg Authigenic* and *Blaser Authigenic* were valid data sets for the Southern and Atlantic oceans, respectively, the extraction protocols for each location should be tested.

4.2. Temporal variation of ε_{Nd} over 520 kyr

4.2.1. Authigenic ε_{Nd} record

The uppermost sample (1.3 ka) at site U1345 has an authigenic ε_{Nd} value of −3.7 ± 0.4 (2σ) (Fig. 5B). It is significantly lower than the core top ε_{Nd} of Fe-Mn oxide from nearby site MR06-04-24 (−1.9 ± 0.4, and −1.4 ± 2.7) (60°15.7′N, 179°25.34′E, 851 m water depth; Asahara et al., 2012). This may be due to the age difference, different sample treatment method and/or recent invasion of volcanic material into the bottom water and *in situ* dissolution. The core top authigenic ε_{Nd} values increase southward. For instance, site U1345 in the mid-Holocene (4.3 ka) (−3.2 ± 0.2) and early-MIS 6 (177 ka) (−3.3 ± 0.2) is less radiogenic than at Bowers Ridge at 5.2 ka (−0.94 ± 0.16) (BOW-8A; Horikawa et al., 2010) or the subarctic N. Pacific (−2.23 ± 0.18, −2.41 ± 0.22 at 180 ka) (13D-27A, 51°27.8′N, 167°38.2′E, 1800-1500 m water depth; van de Flierdt et al., 2004) (Fig. 1). The authigenic ε_{Nd} of U1345 is persistently lower than BOW-8A over the past 145 kyr (Fig. 2). The primary reason seems to be the diminishing influence from unradiogenic N. America with distance.

The average ε_{Nd} of the authigenic fraction over the last 520 kyr is −3.3 ± 0.9 (1σ, n = 98), with large temporal variations (Fig. 5B). Radiogenic ε_{Nd} peaks beyond 1σ (−2.4 to −1.8) occur at the MIS 11/10 boundary, MIS 10, MIS 9, late MIS 8, late MIS 6, the MIS 5/4 boundary, and MIS 4 (dashed vertical lines in Fig. 5). Unradiogenic ε_{Nd} peaks beyond 1σ (−5.6 to −4.1) occur at the MIS 13/12 boundary, early-MIS 12, mid-MIS 12, MIS 7, mid-MIS 6, early-MIS 5, mid-MIS 5, and the MIS 2/1 boundary (dotted vertical lines in Fig. 5). The event at the MIS 2/1 boundary includes four different data points ~1500 years apart. The higher ε_{Nd} signals are associated with cold stages, while the lower ε_{Nd} values occur during warm stages. However, there are exceptions, such as MIS 9 with higher ε_{Nd} and MIS 12 and mid-MIS 6 with lower ε_{Nd}. Horikawa et al. (2010) maintained that radiogenic ε_{Nd} peaks occurred during cold periods over 150 ka, and our ε_{Nd} result generally supports theirs for the past 150 kyr, but the correlation cannot be substantiated beyond that.

4.2.2. Detrital ε_{Nd} record

The average ε_{Nd} of the detrital fraction is −7.8 ± 0.9 (1σ, n = 48) (Fig. 5B). This value is closer to the less radiogenic N. America (ε_{Nd} ~ −10.1 to −8.4) than to the radiogenic Aleutian Arc (ε_{Nd} ~+6 to +10), Kamchatka Arc (ε_{Nd} ~+6 to +9) and Siberia (ε_{Nd} ~ −2 to +3). The lowest ε_{Nd} is −10.3, which is very similar to the Yukon River bedload (−10.1) (data from VanLaningham et al., 2009). The maximum ε_{Nd} is −5.7, indicating an increase in but still minor contribution of the radiogenic Aleutian Arc and Siberia. Unradiogenic ε_{Nd} values (<−8.7) occur in late MIS 10, MIS 7, mid-MIS 6, and at the MIS 2/1 boundary, while radiogenic values (>−6.9) are observed in MIS 11, early MIS 10, MIS 8, and at the MIS 4/3 boundary. The general feature is similar to the authigenic fraction, with a moderate positive correlation between the authigenic and detrital fractions (r^2 = 0.45, n = 40). The correlation is strong (r^2 = 0.51, n = 22) where the ε_{Nd} values of the authigenic fraction are below average (−3.2) but are very weak when they are above average (r^2 = 0.08, n = 18).

4.3. Mechanisms for authigenic ε_{Nd} variation on the Bering Slope

At present, NPIW formation in the Bering Sea is weak (Warner and Roden, 1995). In the absence of NPIW formation, possible

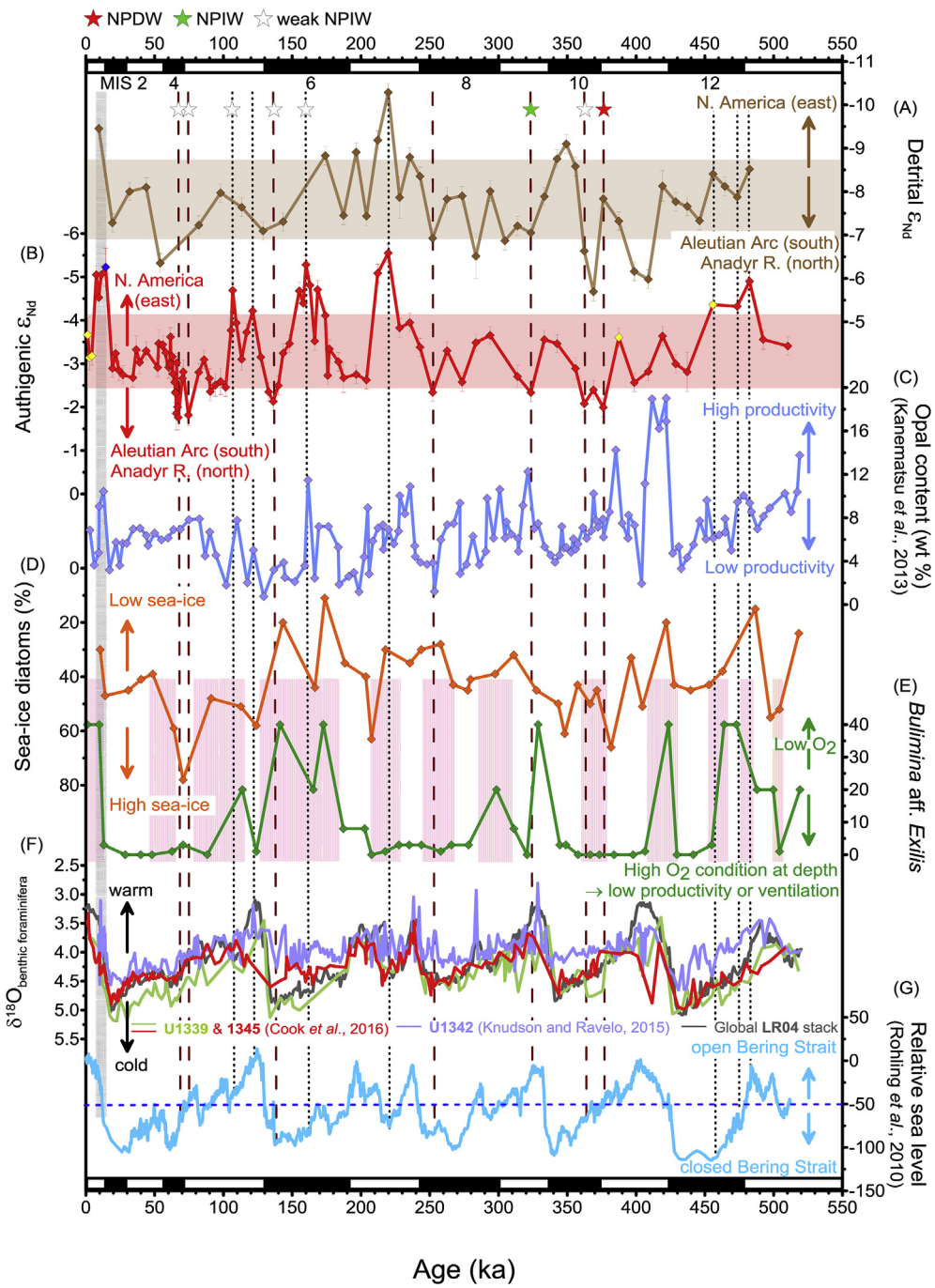

Fig. 5. ε_{Nd} comparison of (A) detrital and (B) authigenic (red: *Wilson Authigenic*, yellow: *Wilson Authigenic* of ash layers, blue: *Rutberg Authigenic*) fractions with (C) opal content (data from Kanematsu et al., 2013); (D) % sea-ice diatoms; (E) *B.* aff. *Exilis* abundance with laminated layer (pink shade); (F) $\delta^{18}O_{bf}$ of U1339, U1345, U1342, and LR04 stack (gray; data from Lisiecki and Raymo, 2005); and (G) relative sea level (data from Rohling et al., 2010). The other proxy data (D, E) are from Expedition 323 Scientists (2011). Dense water formation events are marked with stars (red: NPDW penetration to > 1867 m, green: NPIW penetration to > 1008 m, white: partial NPIW penetration to 1008 m). The brown (in A) and red (in B) shaded areas represent ±1σ variation from the average. (For interpretation of the references to colour in this figure legend, the reader is referred to the web version of this article.)

mechanisms for changing seawater ε_{Nd} at intermediate water depths are (1) lateral advection, (2) boundary exchange (e.g., Arsouze et al., 2007), and (3) pore water diffusion (e.g., Abbott et al., 2015). The Nd of bottom water at site U1345 is a sum of the laterally advected water mass plus the addition from internal sources (the terms in parentheses of Equations (1) and (2) below) as the water mass travels to site U1345.

$$\varepsilon_{Nd,\,U1345} = \varepsilon_{Nd,\,adv} \cdot f_{Nd,\,adv} + \left(\varepsilon_{Nd,\,BE} \cdot f_{Nd,\,BE} + \varepsilon_{Nd,\,pw} \cdot f_{Nd,\,pw}\right) \quad (1)$$

$$f_{Nd,\,adv} + \left(f_{Nd,\,BE} + f_{Nd,\,pw}\right) = 1 \quad (2)$$

where f_{Nd} is the fraction of Nd flux from lateral advection (adv),

boundary exchange (BE), and pore water diffusion (pw).

First, a comparison to the existing ε_{Nd} record at BOW-8A on the Bowers Ridge enables us to apply the two equations. The ε_{Nd} of BOW-8A ranges from −2 to +1 over 150 kyr and is always more radiogenic than site U1345 (Fig. 2). There are two possible interpretations for this ε_{Nd} gap between the two sites. One is that there are two distinct water masses with different ε_{Nd} values. Since the general circulation direction is counter clockwise in the Bering Sea (Fig. 1), the implication is that there is a hydrographic boundary between 884 and 1008 m water depths in the Bering Sea and by extension also in the N. Pacific. However, the potential temperature gradient between the two depths in the N. Pacific (north of 47°N) is less than 0.5 °C (Roemmich and McCallister, 1989 and references therein). The alternative interpretation is that ε_{Nd} is altered along the water circulation path from BOW-8A to U1345 by internal sources. We consider BOW-8A to record the initial water mass value as it travels to site U1345 (Fig. 1), and we used the authigenic ε_{Nd} of BOW-8A (data from Horikawa et al., 2010) for the lateral advection term, $\varepsilon_{Nd,\ adv}$. The ε_{Nd} of internal sources seems to be unradiogenic, since ε_{Nd} becomes more unradiogenic from site BOW-8A to U1345.

The first internal source that we will consider is boundary exchange which "encompasses all chemical transfer reactions among particles and seawater, including adsorption/desorption, ion exchange, and dissolution/precipitation reactions" (Jeandel and Oelkers, 2015). The importance of boundary exchange on the oceanic budget of Nd has been attested to by various field data and model simulations (Arsouze et al., 2007; Lacan and Jeandel, 2001, 2005). Because site U1345 is on the continental margin, it is susceptible to boundary exchange. The dissolution of unradiogenic detrital fractions on the continental margins (Fig. 1) may supply unradiogenic Nd into the bottom water. The decrease in authigenic ε_{Nd} from BOW-8A to U1345 is consistent with this (Section 4.2.1 and Figs. 1 and 2).

The second internal source we will consider pore water diffusion. Pore water diffusion results from Nd liberation during sediment diagenesis and subsequent upward diffusion to the bottom water (Abbott et al., 2015). Abbott et al. (2015) propose two mechanisms that determine the ε_{Nd} of pore water. One is isotopic exchange with reactive authigenic coating. This implies that the ε_{Nd} of pore water is determined by isotopic equilibrium with the past seawater signal (i.e. authigenic coating). For pore water diffusion to supply unradiogenic Nd, older authigenic coatings should be more unradiogenic. However, this is not what is observed in the authigenic record at U1345 (Fig. 2). The other mechanism is preferential dissolution of radiogenic minerals, but if there is preferential dissolution of radiogenic minerals (e.g. Aleutian origin volcanic material) during diagenesis, pore water should supply radiogenic Nd into the bottom water, which is inconsistent with unradiogenic ε_{Nd} shift from BOW-8A to U1345 (Fig. 2). We propose that pore water diffusion is not a primary source for Nd in the Bering Sea.

A comparison of authigenic and detrital ε_{Nd} records at site U1345 (Fig. 5) offers supporting evidence that pore water diffusion is a minor internal source of Nd compared to boundary exchange on the Bering Slope. The similar pattern suggests that detrital ε_{Nd} affects the bottom water ε_{Nd} through boundary exchange. If pore water diffusion were an important additional internal source to bottom water ε_{Nd} (Abbott et al., 2016), one would expect a time lag in the authigenic record, because pore water diffusion liberates past seawater signal captured in authigenic coatings of deposited sediments. The depth below the sediment-water interface where Nd is liberated will vary with the productivity and redox conditions. At present the pore water profile of dissolved Nd concentration (Nd_{pw}) at U1345 is relatively unvarying with depth compared to the heavier REEs which display a large peak below the sulfate-methane transition zone (6.5 CCSF-A (m) from Soyol-Erdene and Huh, 2013) from the reduction of Fe and Mn minerals associated with the anaerobic oxidation of methane. If we take a minor Nd_{pw} peak at 2.5 CCSF-A (m) attributed to the release during organoclastic reduction of Mn oxides, then the estimated time lag is approximately 10 kyrs. We do not observe such time lag in the authigenic record vs. the detrital. Accordingly, we think that boundary exchange is the main mechanism changing seawater ε_{Nd} at this intermediate water depth on the Bering Slope.

We calculated the contribution from boundary exchange ($f_{Nd,\ BE}$) along the Bering Slope using Equations (1) and (2) for two time periods, ~13 ka in the Last Glacial Termination and ~20 ka at the LGM. For simplification, we assumed that the Nd flux from pore water diffusion is insignificant ($f_{Nd,\ pw} \approx 0$). At ~13 ka, we assumed the laterally advected water mass to have $\varepsilon_{Nd,\ adv} = -2$ (from authigenic ε_{Nd} at BOW-8A), boundary exchange on the continental margin to have $\varepsilon_{Nd,\ BE} = -9.5$ (from detrital ε_{Nd} at U1345), and NPIW to have $\varepsilon_{Nd,\ U1345} = -5$ (from authigenic ε_{Nd} at U1345). The result is that ~40% of the bottom water Nd at U1345 is derived from boundary exchange on the continental margin at ~13 ka, which is slightly higher than was estimated for the Madagascan margin (~30% from Wilson et al., 2012). The result for the LGM is slightly lower (~30%), probably due to low sea level conditions. Preferential release of radiogenic Nd by boundary exchange is not considered here (Noble et al., 2013; Wilson et al., 2012), and detrital ε_{Nd} on the eastern part of the Bering shelf is more radiogenic than what we assumed for $\varepsilon_{Nd,\ BE}$ (Fig. 1), so the contribution from boundary exchange is a lower estimate. If we assume the water transport time from BOW-8A to U1345 to be 200 years (maximum estimate from modeling of ^{14}C data; Matsumoto, 2007), the maximum water residence time for Nd is ~700 years, broadly consistent with currently accepted values (Tachikawa et al., 1999).

In the absence of NPIW formation, we propose that boundary exchange is the main mechanism that influences the Nd isotopic composition in the Bering Sea, with a minor contribution from pore waters. It is important to note that boundary exchange processes supply unradiogenic Nd, and hence, NPIW formation is the main mechanism that can introduce radiogenic Nd to site U1345.

4.4. NPIW formation

It is likely that NPIW formed by brine rejection during sea ice formation (e.g., Haley et al., 2007; Jang et al., 2013). Being at the edge of the present-day maximum sea ice extent, there is potential for intensified brine formation at site U1345 (Rella et al., 2012). A useful proxy in this regard is $\Delta\delta^{18}O_{bf}$, the $\delta^{18}O_{bf}$ difference between sites at different water depths (sites U1339, U1342 and U1345) (Fig. 5F). Indeed, the $\Delta\delta^{18}O_{bf}$ values attest to periods of brine rejection within the Bering Sea (Cook et al., 2016; Knudson and Ravelo, 2015). For example, the glacial $\delta^{18}O_{bf}$ at site U1339 (54°40N, 169°59W; eastern Bering Slope) at a water depth of 1867 m is 0.4–0.8‰ lighter than at site U1342 (54°50N, 176°55W; Bowers Ridge) at a water depth of 818 m (Cook et al., 2016). This is larger than the difference at present (~0.3‰), suggesting that brine rejection delivered the extremely low-$\delta^{18}O$ surface water to greater depths during the glacial (Brennan et al., 2013; Hillaire-Marcel and de Vernal, 2008).

Neodymium isotopic composition records more "local" NPIW events. We observe a few time intervals where $\delta^{18}O_{bf}$ gradients between sites U1339 and U1345 are larger than at present (Fig. 5F); however, not all of them have coincident ε_{Nd} excursions (e.g., MIS 2). One possible explanation is that NPIW did not originate in the Bering Sea. Let us suppose that NPIW forms by brine rejection in the Okhotsk Sea and flows into the Bering Sea. This water mass transfers light $\delta^{18}O$ to the Bering Sea, but the ε_{Nd} of the water mass

is modified by boundary exchange during transit due to the short residence time of Nd (Tachikawa et al., 1999) (see Section 4.3). Alternatively, if the ε_{Nd} of the sinking surface water is similar to that of the bottom water, the ε_{Nd} of the bottom water would not change even though NPIW forms. A third possibility is that the ε_{Nd} change by NPIW formation is muted when other Nd sources change the ε_{Nd} value in the opposite direction. Whichever the case may be, the Nd isotopic composition has an advantage in recording "local" NPIW formation events in the Bering Sea and pinpointing its source, although it may not record all events. This proxy can also provide ancillary information about boundary exchange.

Here, we focus on the ε_{Nd} variations to trace local NPIW formation on the Bering Slope and to constrain other Nd sources. We compare ε_{Nd} with biological proxies such as $\Delta\delta^{18}O_{bf}$ values, opal content, % sea-ice related diatoms, and the abundance of *B. aff. Exilis*. The $\delta^{18}O_{bf}$ values of sites U1339, U1342 and U1345 provide a perspective on the water mass properties at different depths (data for U1339 and U1345 from Cook et al., 2016; data for U1342 from Knudson and Ravelo, 2015). In particular, a large $\Delta\delta^{18}O_{bf}$ reflects the occurrence of brine rejection from shallower depths. The opal content is used as an indicator of biological productivity here, with the high opal content typically associated with low GRA bulk density, low NGR count, and high color reflectance b* value (not shown). Sea-ice related diatoms include *T. antarctica* spores, *B. fragilis*, *D. confervacea*, *T. hyalina*, *P. glacialis* and *F. cylindrus* (data from Expedition 323 Scientists, 2011). They can trace sea ice expansion in the Bering Sea. Considering the trace amount of brine rejection at present (Warner and Roden, 1995), NPIW formation may have occurred when the percentage of sea-ice diatoms was higher than the modern value of 30%. *B. aff. Exilis* is one of the benthic foraminifera species (data from Expedition 323 Scientists, 2011) that has been used to indicate low oxygen conditions at depth (Bubenshchikova et al., 2008; Kaiho, 1994). At present, low ventilation and enhanced biological respiration accompanying high productivity cause *B. aff. Exilis* to flourish. On the other hand, low productivity and/or vigorous ventilation processes can reduce *B. aff. Exilis*.

4.4.1. Periods of radiogenic Nd input

We can attribute the radiogenic ε_{Nd} peaks to either NPIW formation from radiogenic surface water, a decrease in the extent of boundary exchange supplying unradiogenic Nd (Section 4.3), or a combination of the two. Seawater that has circulated past the Anadyr River mouth and/or the Aleutian Arc can supply radiogenic Nd. At present, the Anadyr River water mainly flows through the Bering Strait into the Arctic Ocean, but model simulations suggest that it diverts into the Bering Sea if the Strait is closed (Hu et al., 2012b). All radiogenic events except for MIS 9 occur when the Bering Strait is nearly or completely closed, and in such cases, the Anadyr River is a possible additional radiogenic source (Fig. 5G, dashed vertical lines). We rule out the contribution from Kamchatka, because that water mass mainly flows out along the western boundary to the N. Pacific regardless of sea level (Hu et al., 2012b). We will examine the seven radiogenic ε_{Nd} periods in four categories, starting with the proposed NPDW formation at the MIS 11/10 boundary, the NPIW formation at MIS 9, and the weak NPIW formation at MIS 10 and 6, the MIS 5/4 boundary and MIS 4 (Fig. 5). Finally, there is no dense water formation at MIS 8.

The event at the MIS 11/10 boundary is possibly related to NPDW formation. The similar $\delta^{18}O_{bf}$ values at sites U1339, 1342, and 1345 indicate homogeneity of the water column between 818 and 1867 m depths. The $\delta^{18}O_{bf}$ are ~0.2‰ lighter than the global LR04 stack, suggesting input of light surface water all the way down to 1867 m (Fig. 5F). High % sea-ice diatoms and low *B. aff. Exilis* support dense water formation triggered by brine formation (Fig. 5D and E). Because the sea level was relatively low, the Anadyr River was an additional radiogenic source (Fig. 5G). Dynamic ocean circulation triggered by dense water formation probably decreased exposure time for boundary exchange and limited its effect (Siddall et al., 2008; Stewart et al., 2016). Hence, the radiogenic ε_{Nd} value at the MIS 11/10 boundary results from NPDW formation entraining radiogenic Nd and weakened unradiogenic Nd input.

The radiogenic signal during the peak interglacial at MIS 9 is an example of NPIW formation. The $\delta^{18}O_{bf}$ value of site U1345 is similar to that of site U1342 and is ~0.6‰ lower than that of site U1339 (Fig. 5F). This means that the water column between 818 and 1008 m was homogenous and that the hydrographic boundary lay between 1008 and 1867 m, i.e., brine intruded to at least a ~1008 m depth. Higher-than-modern % sea-ice diatoms are consistent with this interpretation (Fig. 5D). *B. aff. Exilis* decreases (Fig. 5E), and the opal content increases during the same period (Fig. 5C). The unradiogenic input from boundary exchange was probably reduced due to the short exposure time.

The radiogenic events at MIS 10 and 6, the MIS 5/4 boundary, and MIS 4 result from weak NPIW formation. During these events, the $\delta^{18}O_{bf}$ values at site U1345 are between those at sites U1339 and 1342: they are 0.30–0.35‰ lighter than at site U1339 and 0.15–0.50‰ heavier than at site U1342 (Fig. 5F). This suggests that surface water only partially penetrated to ~1008 m. High % sea-ice diatoms and low *B. aff. Exilis* support brine-induced NPIW formation—Late MIS 6 is an exception, as it may be an artifact of the low sample resolution (Fig. 5D and E). At these times, the sea level was low, and the nearly or completely closed Bering Strait implies inflow of the Anadyr River component in addition to the usual Aleutian Arc component (Fig. 5G). Model simulations predict a reduction in the Yukon River discharge by 78% during glacial periods. It can promote NPIW formation by increasing surface water salinity (Kim and Park, 2008). The diminished ε_{Nd} gap between sites U1345 and BOW-8A at MIS 4 supports the radiogenic NPIW formation on the Bering Slope as well as weakened unradiogenic flux due to the short exposure time (Fig. 2, blue bar).

Whether NPIW formed at MIS 8 is highly uncertain. The $\delta^{18}O_{bf}$ value at site U1345 is indistinguishable from that at site U1339 but is significantly heavier than at site U1342 (~0.9‰) (Fig. 5F). This means that NPIW, if present, occupied a water depth shallower than ~1008 m and that the water column between ~1008 and 1867 m was homogeneous. The low abundance of *B. aff. Exilis* can be attributed to the low oxygen consumption rather than to ventilation processes (Fig. 5E), which is consistent with the low opal content. The relatively radiogenic ε_{Nd} of detrital fractions (Fig. 5A) implies that boundary exchange supplied radiogenic Nd.

In summary, we suggest that most radiogenic ε_{Nd} excursions record dense water formation such as NPIW and NPDW except for MIS 8 (Fig. 6A). The most probable sources for radiogenic Nd are the inflow from the Anadyr River and the Aleutian Arc, which penetrate to greater depths *via* brine formation. The radiogenic ε_{Nd} excursions during MIS 8 may be due to boundary exchange with radiogenic detrital material rather than formation of NPIW. The relationship between NPIW/NPDW formation and the closure of the Bering Strait as suggested by Knudson and Ravelo (2015) is circumstantial. Exceptionally, NPIW formation occurred at MIS 9, when the sea level was comparable to that of the present.

4.4.2. Periods of unradiogenic Nd input

The unradiogenic peaks result from an increase in NPIW formation from unradiogenic surface water, an increase in boundary exchange, or a combination of the two. The probable unradiogenic source to surface water is riverine or groundwater input from N. America, which is stronger during warm periods (Kim and Park, 2008). Under higher sea level conditions, the unradiogenic

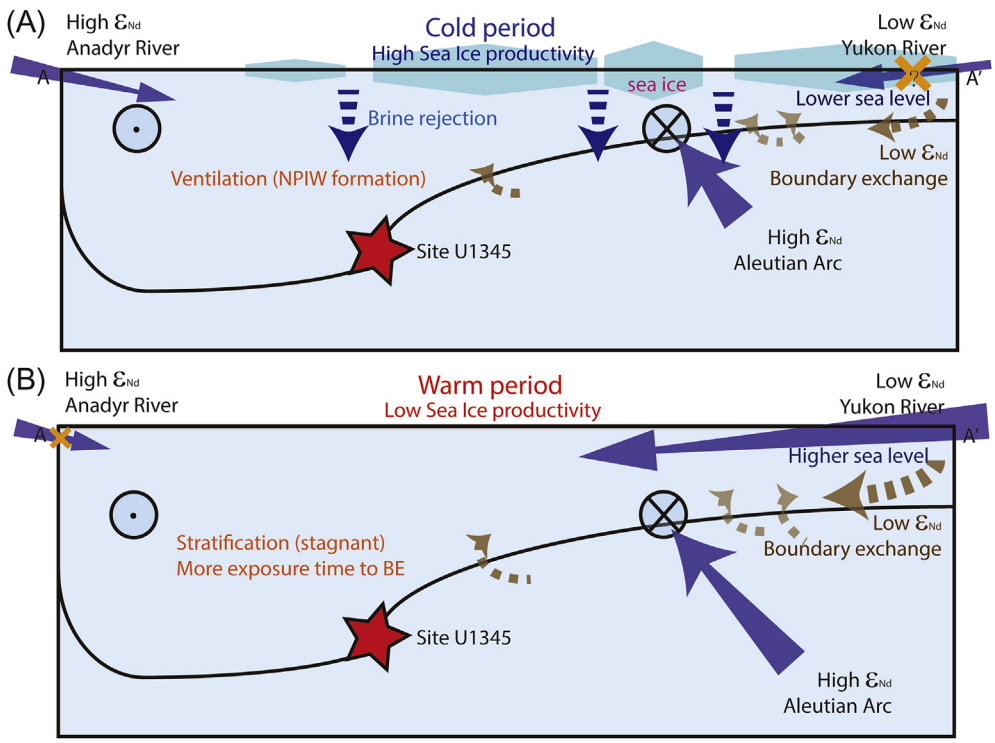

Fig. 6. Schematic illustration of ocean circulation in the Bering Sea during typical low (A) and high (B) sea ice productivity conditions across the A-A′ transect marked in Fig. 1. During cold periods, enhanced sea ice production can trigger NPIW formation through brine rejection, causing the sinking of water masses containing radiogenic Nd. Mid-MIS 6 and mid-MIS 5 are exceptions, when unradiogenic ε_{Nd} from N. America reached the Bering Sea and participated in NPIW formation. During warm periods, boundary exchange (BE) can supply unradiogenic Nd under stagnant bottom water conditions. In case of MIS 8, preferential release of reactive particulate matter is probable.

character is accentuated due to the lack of input from the Anadyr River. The six unradiogenic ε_{Nd} periods will be discussed in two categories, starting with NPIW formation in the mid-MIS 6 and mid-MIS 5 and no dense water formation at the MIS 13/12 boundary, early-MIS 12, mid-MIS 12, and MIS 7 (Fig. 5).

We consider the unradiogenic events in mid-MIS 6 and mid-MIS 5 to be partially influenced by NPIW formation. The situation is similar to the radiogenic event at MIS 10. A decreasing trend of $\delta^{18}O_{bf}$ from deep (U1339) to shallow (U1342) sites is observed, with site U1345 0.3–0.4‰ lighter than site U1339 and 0.2–0.3‰ heavier than U1342. This suggests that a portion of the surface water sank to ~1008 m. Brine formation is probable, based on the higher % sea-ice diatoms than present (Fig. 5D). *B. aff. Exilis* is abundant, although lower than at present. Intermediate to high opal productivity may cause low oxygen conditions even with partial ventilation, or this may be an artifact of the low sample resolution. The relatively low ε_{Nd} of the detrital fraction indicates that NPIW formation in mid-MIS 6 and mid-MIS 5 had unradiogenic Nd sources (Fig. 5A).

The unradiogenic events at the MIS 13/12 boundary, early-MIS 12, mid-MIS 12, and MIS 7 probably transpired through boundary exchange rather than NPIW formation (Fig. 6B). The $\delta^{18}O_{bf}$ values at site U1345 are similar to those of site U1339 at those times but are significantly heavier than at site U1342 (0.3–0.7‰) (Fig. 5F). The percent sea-ice diatoms are similar to those of the present. This implies the absence of NPIW formation at ~1008 m. The oxygen-poor environment indicated by high *B. aff. Exilis* and/or lamination at those times is consistent with this implication (Fig. 5E). MIS 7 is an exception with low *B. aff. Exilis* and yet has lamination. The boundary exchange process may provide more unradiogenic Nd, considering the lower ε_{Nd} of the detrital fractions than average at those times (Fig. 5A) and stagnant bottom water conditions in the absence of dense water formation (Siddall et al., 2008; Stewart et al., 2016).

We do not evaluate the unradiogenic events in early-MIS 5 and at the MIS 2/1 boundary. The $\delta^{18}O_{bf}$ value of site U1345 in early-MIS 5 is 0.3 and is ~1‰ heavier than U1339 and U1342, respectively. This inverse $\delta^{18}O_{bf}$ feature between sites U1345 and U1339 may be attributed to age uncertainty due to poor microfossil preservation in U1345 (Cook et al., 2016). The event at the MIS 2/1 boundary is more complicated. It includes four unradiogenic ε_{Nd} data points associated with different $\Delta\delta^{18}O_{bf}$ features: partial NPIW (similar to mid-MIS 5), inverse $\Delta\delta^{18}O_{bf}$ (similar to early-MIS 5), no NPIW (similar to MIS 7), and inverse $\Delta\delta^{18}O_{bf}$ again, consecutively. This ambiguous $\Delta\delta^{18}O_{bf}$ series may reflect abrupt climate change during deglaciation or age uncertainty (several thousand years; Cook et al., 2016).

In summary, the Nd isotopic composition can trace "local" dense water formation on the Bering Slope when ε_{Nd} of surface water is distinct from that of deep water. We can detect NPIW/NPDW formation at the MIS 11/10 boundary, in MIS 10 and 9, mid and late-MIS 6, mid-MIS 5, at the MIS 5/4 boundary, and in MIS 4. Considering $\Delta\delta^{18}O_{bf}$ between three sites (U1339, U1342, and U1345), we can estimate the intrusion depths (star symbols in Fig. 5). Whereas NPIW was observed regularly during extreme glacials (closed Bering Strait) at the relatively shallow U1342 (Knudson and Ravelo, 2015), NPIW episodes were short and did not regularly occur during all extreme glacials at the deeper U1345. This difference results from variation in the intrusion depth of NPIW, so the events detected by ε_{Nd} at site U1345 indicate more vigorous ventilation.

4.4.3. Relationship between NPIW and NADW

We examine the hypothesis concerning alternating strengths of NPIW and NADW (the seesaw hypothesis) by comparing the ε_{Nd} of the Bering Slope (site U1345) and the South Atlantic (Fig. 7). The S.

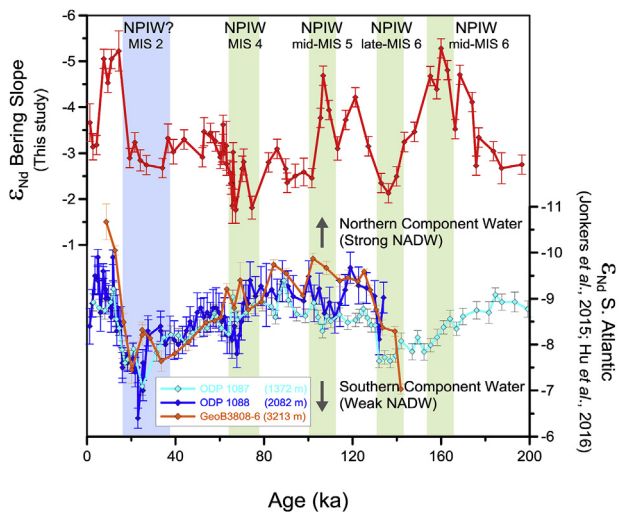

Fig. 7. Comparison of the authigenic ε_{Nd} records for the Bering Slope and the South Atlantic to examine the NPIW-NADW Seesaw Hypothesis. NPIW events at site U1345 are compared with the strength of NADW recorded in GeoB (orange), ODP 1088 (blue) and 1087 (sky blue). The NPIW events discussed in Section 4.4 are marked with green bars. At the LGM, ε_{Nd} does not record an NPIW event, but $\Delta\delta^{18}O_{bf}$ on the Bering Slope indicates a seesaw (blue bar). (For interpretation of the references to colour in this figure legend, the reader is referred to the web version of this article.)

Atlantic records are from cores GeoB3808-6 (30.8°S, 14.7°W; 3213 m water depth), ODP 1088 (41.8°S, 13.3°E; 2082 m water depth) and ODP 1087 (31.3°S, 15.2°E; 1372 m water depth), which extend to 145 ka (Jonkers et al., 2015), 135 ka and 200 ka, respectively (Hu et al., 2016). The deeper sites GeoB3808 and ODP 1088 are currently bathed by the lower and upper NADW, respectively, and are well suited to monitor the varying strength of NADW. ODP 1087 is somewhat shallower but displays very similar ε_{Nd} pattern to ODP 1088 during cold period such as MIS 4 and 2 (Hu et al., 2016). Thus, as GeoB3808 and ODP 1088 do not extend to MIS 6, we used ODP 1087 to gain a perspective on the ε_{Nd} variation beyond 145 ka. The low (high) ε_{Nd} of S. Atlantic cores result from northern (southern) component water and indicates strong (weak) NADW formation.

The four NPIW periods over the last 200 kyrs in the Bering Sea coincided with periods of NADW reduction (Fig. 7). The NPIW formation with radiogenic excursions in late MIS 6 and MIS 4 on the Bering Slope coincides with the reduction in NADW, as do less certain events with unradiogenic ε_{Nd} in mid MIS 6 and mid-MIS 5. At those times, NPIW may have regulated the global climate system as a reservoir for carbon dioxide and as heat distributor. However, NADW reduction in mid-MIS 5 is only detected on ODP 1088 with 1.1 ε_{Nd} shift, and NADW variation recorded in GeoB3808 is relatively small. This site-dependent seesaw is probably due to the modest NADW change in mid-MIS 5 (Hu et al., 2016), different water mass source in the eastern and western basins of Atlantic Ocean (Oliver et al., 2010) or low sampling resolution in GeoB3808. We do not detect NPIW formation on the Bering Slope during the LGM when NADW formation is strongly reduced. Considering the low $\delta^{18}O_{bf}$ during the LGM (Cook et al., 2016), NPIW may have formed in other N. Pacific sites, or the ε_{Nd} records on NPIW formation in the Bering Sea may be muted by boundary exchange (see Section 4.4). In summary, the strength of NPIW is generally anti-correlated with that of NADW, supporting the seesaw hypothesis (e.g. Hu et al., 2012a; Okazaki et al., 2010; Saenko et al., 2004), but we could not resolve the NPIW-NADW seesaw across all climate transitions. An extended authigenic ε_{Nd} record in the Atlantic Ocean would be desirable for comparison to our record.

5. Conclusion

We reconstructed a 520-kyr record of the neodymium isotope ratio of the bottom water on the Bering Slope using the bulk sediment leachates. To establish the reliability of the data, we examined six different fractions for their Nd isotopic composition and elemental concentrations, such as Al, Fe, Mn, Sr, and REEs. The six fractions were the carbonate fraction, the three Fe-Mn oxyhydroxide fractions extracted by three different conventional methods, the second bulk sediment leachate, and the detrital fraction. Relatively low ε_{Nd} values suggest that omitting the carbonate removal step and adopting a low reagent-to-sediment ratio proved to be the most reliable method to recover bottom water composition in the Bering Sea. Therefore, a site-specific adaptation or test of the leaching protocol is necessary.

The reconstructed bottom water ε_{Nd} at site U1345 shows two features: radiogenic ε_{Nd} peaks and unradiogenic ε_{Nd} troughs. The authigenic ε_{Nd} variations represent an interplay between North Pacific Intermediate Water (NPIW) formation and boundary exchange. The radiogenic ε_{Nd} values seems to result from the dense water formation containing radiogenic Nd. Enhanced sea ice can trigger brine formation, and consequent NPIW can transport radiogenic Nd from the surface to depth. Such dynamic bottom water conditions can reduce the contact time between unradiogenic sediments and overlying water, resulting in diminished boundary exchange and enhanced radiogenic peaks. The magnitude of NPIW remains uncertain given available data. The unradiogenic ε_{Nd} events are primarily affected by boundary exchange processes. In the absence of NPIW formation, the contact time between sediments and overlying water should be longer, and hence unradiogenic Nd input from boundary exchange seems to be stronger. Exceptionally, the unradiogenic events in mid-MIS 6 and mid-MIS 5 may still be related to NPIW formation.

The first bottom water ε_{Nd} reconstruction in the Bering Sea covering the last 520 kyr allows us to evaluate the NPIW-North Atlantic Deep Water (NADW) seesaw hypothesis suggested by many models (Hu et al., 2015; Okazaki et al., 2010). A tentative comparison with ε_{Nd} records from the S. Atlantic sites GeoB3808, ODP 1088 and ODP 1087 covering the last 200 kyr suggests that the NPIW formation in the Bering Sea played an important role in sequestering CO_2 into the bottom water and in regulating the global heat distribution when NADW was reduced during mid-MIS 6, late-MIS 6, mid-MIS 5 and MIS 4. Obtaining an extended authigenic ε_{Nd} record in the Atlantic Ocean will allow us to evaluate the seesaw hypothesis more fully.

Acknowledgements

This research was supported by the NRF Mid-Career Researcher Program (NRF-2011-0015174) and Basic Science Research Program (NRF-2014R1A1A3049836) funded by MSIP, Korea; the Gas Hydrate and Paleoceanographic Reconstruction in the Western Arctic Ocean (PE16062) and a KOPRI research grant (PE16010) funded by MOF, Korea; and the Integrated Ocean Drilling Program funded by the MLTMA, Korea. We thank M. Cook and K. Knudson for sharing oxygen isotope data, and H. Ashahi, K. Takahashi, B. Caissie for discussions on the age model and the sediment core, and J.S. Ryu and C. Han for helping with instrumental analysis. Comments from the editor and two anonymous reviewers helped improve the manuscript.

Appendix A. Supplementary data

Supplementary data related to this article can be found at http://dx.doi.org/10.1016/j.quascirev.2016.11.032.

References

Abbott, A.N., Haley, B.A., McManus, J., 2015. Bottoms up: sedimentary control of the deep North Pacific Ocean's ε_{Nd} signature. Geology 43, 1035–1035.

Abbott, A.N., Haley, B.A., McManus, J., 2016. The impact of sedimentary coatings on the diagenetic Nd flux. Earth Planet. Sci. Lett. 449, 217–227.

Akagi, T., Yasuda, S., Asahara, Y., Emoto, M., Takahashi, K., 2014. Diatoms spread a high ε_{Nd}-signature in the North Pacific Ocean. Geochem. J. 48, 121–131.

Albarède, F., Goldstein, S.L., 1992. World map of Nd isotopes in sea-floor ferromanganese deposits. Geology 20, 761–763.

Albarède, F., Goldstein, S.L., Dautel, D., 1997. The neodymium isotopic composition of manganese nodules from the Southern and Indian oceans, the global oceanic neodymium budget, and their bearing on deep ocean circulation. Geochim. Cosmochim. Acta 61, 1277–1291.

Arsouze, T., Dutay, J.-C., Lacan, F., Jeandel, C., 2007. Modeling the neodymium isotopic composition with a global ocean circulation model. Chem. Geol. 239, 165–177.

Asahara, Y., Takeuchi, F., Nagashima, K., Harada, N., Yamamoto, K., Oguri, K., Tadai, O., 2012. Provenance of terrigenous detritus of the surface sediments in the Bering and Chukchi Seas as derived from Sr and Nd isotopes: implications for recent climate change in the Arctic regions. Deep-Sea Res. II 61–64, 155–171.

Axelsson, M.D., Rodushkin, I., Ingri, J., Öhlander, B., 2002. Multielemental analysis of Mn–Fe nodules by ICP-MS: optimisation of analytical method. Analyst 127, 76–82.

Bayon, G., Barrat, J.A., Etoubleau, J., Benoit, M., Bollinger, C., Révillon, S., 2009. Determination of rare earth elements, Sc, Y, Zr, Ba, Hf and Th in geological samples by ICP-MS after Tm addition and alkaline fusion. Geostand. Geoanal. Res. 33, 51–62.

Bayon, G., German, C.R., Boella, R.M., Milton, J.A., Taylor, R.N., Nesbitt, R.W., 2002. An improved method for extracting marine sediment fractions and its application to Sr and Nd isotopic analysis. Chem. Geol. 187, 179–199.

Biastoch, A., Böning, C.W., Getzlaff, J., Molines, J.-M., Madec, G., 2008. Causes of interannual-decadal variability in the meridional overturning circulation of the midlatitude North Atlantic Ocean. J. Clim. 21, 6599–6615.

Blaser, P., Lippold, J., Gutjahr, M., Frank, N., Link, J.M., Frank, M., 2016. Extracting foraminiferal seawater Nd isotope signatures from bulk deep sea sediment by chemical leaching. Chem. Geol. 439, 189–204.

Brennan, C., Meissner, K., Eby, M., Hillaire-Marcel, C., Weaver, A., 2013. Impact of sea ice variability on the oxygen isotope content of seawater under glacial and interglacial conditions. Paleoceanography 28, 388–400.

Bubenshchikova, N., Nürnberg, D., Lembke-Jene, L., Pavlova, G., 2008. Living benthic foraminifera of the Okhotsk Sea: faunal composition, standing stocks and microhabitats. Mar. Micropaleontol. 69, 314–333.

Cook, M.S., Ravelo, A.C., Mix, A., Nesbitt, I.M., Miller, N.V., 2016. Tracing subarctic Pacific water masses with benthic foraminiferal stable isotopes during the LGM and late Pleistocene. Deep-Sea Res. II 125, 84–95.

Expedition 323 Scientists, 2011. Site U1345. In: Takahashi, K., Ravelo, A.C., Alvarez Zarikian, C.A. (Eds.), The Expedition 323 Scientists, Proc. IODP, vol. 323. Integrated Ocean Drilling Program Management International, Inc., Tokyo.

Frank, M., Whiteley, N., Kasten, S., Hein, J.R., O'Nions, K., 2002. North Atlantic deep water export to the Southern Ocean over the past 14 Myr: evidence from Nd and Pb isotopes in ferromanganese crusts. Paleoceanography 17, 1022–1030.

GEOROC, 2003. Geochemistry of Rocks of the Oceans and Continents. Max-Planck Institute fur Chemie, Mainz, Germany. http://georoc.mpch-mainz.gwdg.de/.

Gutjahr, M., Frank, M., Stirling, C.H., Klemm, V., van de Flierdt, T., Halliday, A.N., 2007. Reliable extraction of a deepwater trace metal isotope signal from Fe-Mn oxyhydroxide coatings of marine sediments. Chem. Geol. 242, 351–370.

Häkkinen, S., Rhines, P.B., 2004. Decline of subpolar North Atlantic circulation during the 1990s. Science 304, 555–559.

Haley, B.A., Frank, M., Spielhagen, R.F., Eisenhauer, A., 2007. Influence of brine formation on Arctic Ocean circulation over the past 15 million years. Nat. Geosci. 1, 68–72.

Haley, B.A., Polyak, L., 2013. Pre-modern Arctic Ocean circulation from surface sediment neodymium isotopes. Geophys. Res. Lett. 40, 893–897.

Heimburger, A., Losno, R., Triquet, S., Nguyen, E.B., 2013. Atmospheric deposition fluxes of 26 elements over the Southern Indian Ocean: time series on Kerguelen and Crozet Islands. Glob. Biogeochem. Cy 27, 440–449.

Hein, J.R., O'Neil, J.R., Jones, M.G., 1979. Origin of authigenic carbonates in sediment from the deep Bering Sea. Sedimentology 26, 681–705.

Hillaire-Marcel, C., de Vernal, A., 2008. Stable isotope clue to episodic sea ice formation in the glacial North Atlantic. Earth Planet. Sci. Lett. 268, 143–150.

Horikawa, K., Asahara, Y., Yamamoto, K., Okazaki, Y., 2010. Intermediate water formation in the Bering Sea during glacial periods: evidence from neodymium isotope ratios. Geology 38, 435–438.

Hu, A., Meehl, G.A., Han, W., Abe-Ouchi, A., Morrill, C., Okazaki, Y., Chikamoto, M.O., 2012a. The Pacific-Atlantic seesaw and the Bering Strait. Geophys. Res. Lett. 39, L03702 doi: 03710.01029/02011GL050567.

Hu, A., Meehl, G.A., Han, W., Otto-Bliestner, B., Abe-Ouchi, A., Rosenbloom, N., 2015. Effects of the Bering Strait closure on AMOC and global climate under different background climates. Prog. Oceanogr. 132, 174–196.

Hu, A., Meehl, G.A., Han, W., Timmermann, A., Otto-Bliesner, B., Liu, Z., Washington, W.M., Large, W., Abe-Ouchi, A., Kimoto, M., 2012b. Role of the Bering Strait on the hysteresis of the ocean conveyor belt circulation and glacial climate stability. Proc. Natl. Acad. Sci. 109, 6417–6422.

Hu, R., Noble, T.L., Piotrowski, A.M., McCave, I.N., Bostock, H.C., Neil, H.L., 2016. Neodymium isotopic evidence for linked changes in Southeast Atlantic and Southwest Pacific circulation over the last 200 kyr. Earth Planet. Sci. Lett. 455, 106–114.

Jacobsen, S.B., Wasserburg, G.J., 1980. Sm-Nd isotopic evolution of chondrites. Earth Planet. Sci. Lett. 50, 139–155.

Jang, K., Han, Y., Huh, Y., Nam, S.-I., Stein, R., Mackensen, A., Matthiessen, J., 2013. Glacial freshwater discharge events recorded by authigenic neodymium isotopes in sediments from the Mendeleev Ridge, western Arctic Ocean. Earth Planet. Sci. Lett. 369–370, 148–157.

Jauhari, P., Pattan, J.N., 2000. Ferromanganese nodules from the central Indian Ocean basin. In: Cronan, D.S. (Ed.), Handbook of Marine Mineral Deposits. CRC Press, pp. 171–195.

Jeandel, C., Oelkers, E.H., 2015. The influence of terrigenous particulate material dissolution on ocean chemistry and global element cycles. Chem. Geol. 395, 50–66.

Jonkers, L., Zahn, R., Thomas, A., Henderson, G., Abouchami, W., François, R., Masque, P., Hall, I.R., Bickert, T., 2015. Deep circulation changes in the central South Atlantic during the past 145 kyrs reflected in a combined $^{231}Pa/^{230}Th$, neodymium isotope and benthic $\delta^{13}C$ record. Earth Planet. Sci. Lett. 419, 14–21.

Kaiho, K., 1994. Benthic foraminiferal dissolved-oxygen index and dissolved-oxygen levels in the modern ocean. Geology 22, 719–722.

Kanematsu, Y., Takahashi, K., Kim, S., Asahi, H., Khim, B.-K., 2013. Changes in biogenic opal productivity with Milankovitch cycles during the last 1.3 Ma at IODP Expedition 323 Sites U1341, U1343, and U1345 in the Bering Sea. Quatern. Int. 310, 213–220.

Katsuki, K., Takahashi, K., 2005. Diatoms as paleoenvironmental proxies for seasonal productivity, sea-ice and surface circulation in the Bering Sea during the late Quaternary. Deep-Sea Res. II 52, 2110–2130.

Kim, S.J., Park, Y.G., 2008. Glacial ocean circulation and property changes in the North Pacific. Atmos. Ocean. 46, 257–275.

Knudson, K.P., Ravelo, A.C., 2015. North Pacific Intermediate Water circulation enhanced by the closure of the Bering Strait. Paleoceanography 30, 1287–1304.

Lacan, F., Jeandel, C., 2001. Tracing Papua New Guinea imprint on the central Equatorial Pacific Ocean using neodymium isotopic compositions and Rare Earth Element patterns. Earth Planet. Sci. Lett. 186, 497–512.

Lacan, F., Jeandel, C., 2005. Neodymium isotopes as a new tool for quantifying exchange fluxes at the continent–ocean interface. Earth Planet. Sci. Lett. 232, 245–257.

Lisiecki, L.E., Raymo, M.E., 2005. A Plio-Pleistocene stack of 57 globally distributed benthic $\delta^{18}O$ records. Paleoceanography 20, PA1003 doi: 1010.1029/2004PA001071.

Míková, J., Denková, P., 2007. Modified chromatographic separation scheme for Sr and Nd isotope analysis in geological silicate samples. J. Geosci. 221–226.

Martin, E., Scher, H., 2004. Preservation of seawater Sr and Nd isotopes in fossil fish teeth: bad news and good news. Earth Planet. Sci. Lett. 220, 25–39.

Martin, E.E., Blair, S.W., Kamenov, G.D., Scher, H.D., Bourbon, E., Basak, C., Newkirk, D.N., 2010. Extraction of Nd isotopes from bulk deep sea sediments for paleoceanographic studies on Cenozoic time scales. Chem. Geol. 269, 414–431.

Matsumoto, K., 2007. Radiocarbon-based circulation age of the world oceans. J. Geophys. Res. Oceans 112, C09004 doi: 09010.01029/02007JC004095.

Max, L., Lembke-Jene, L., Riethdorf, J.-R., Tiedemann, R., Nürnberg, D., Kühn, H., Mackensen, A., 2014. Pulses of enhanced North Pacific Intermediate Water ventilation from the Okhotsk Sea and Bering Sea during the last deglaciation. Clim. Past. 10, 591–605.

Noble, T.L., Piotrowski, A.M., McCave, I.N., 2013. Neodymium isotopic composition of intermediate and deep waters in the glacial southwest Pacific. Earth Planet. Sci. Lett. 384, 27–36.

Ohkushi, K.i., Itaki, T., Nemoto, N., 2003. Last Glacial–Holocene change in intermediate-water ventilation in the Northwestern Pacific. Quat. Sci. Rev. 22, 1477–1484.

Okazaki, Y., Timmermann, A., Menviel, L., Harada, N., Abe-Ouchi, A., Chikamoto, M.O., Mouchet, A., Asahi, H., 2010. Deepwater formation in the North Pacific during the last glacial termination. Science 329, 200–204.

Oliver, K.I.C., Hoogakker, B.A.A., Crowhurst, S., Henderson, G.M., Rickaby, R.E.M., Edwards, N.R., Elderfield, H., 2010. A synthesis of marine sediment core $\delta^{13}C$ data over the last 150,000 years. Clim. Past. 6, 645–673.

Pin, C., Zalduegui, J.S., 1997. Sequential separation of light rare-earth elements, thorium and uranium by miniaturized extraction chromatography: Application to isotopic analyses of silicate rocks. Anal. Chim. Acta 339, 79–89.

Rella, S.F., Tada, R., Nagashima, K., Ikehara, M., Itaki, T., Ohkushi, K.I., Sakamoto, T., Harada, N., Uchida, M., 2012. Abrupt changes of intermediate water properties on the northeastern slope of the Bering Sea during the last glacial and deglacial period. Paleoceanography 27, PA3203 doi: 3210.1029/2011PA002205.

Roberts, N.L., Piotrowski, A.M., McManus, J.F., Keigwin, L.D., 2010. Synchronous deglacial overturning and water mass source changes. Science 327, 75–78.

Roemmich, D., McCallister, T., 1989. Large scale circulation of the North Pacific Ocean. Prog. Oceanogr. 22, 171–204.

Rohling, E.J., Braun, K., Grant, K., Kucera, M., Roberts, A.P., Siddall, M., Trommer, G., 2010. Comparison between Holocene and Marine Isotope Stage-11 sea-level histories. Earth Planet. Sci. Lett. 291, 97–105.

Rutberg, R.L., Hemming, S.R., Goldstein, S.L., 2000. Reduced North Atlantic Deep Water flux to the glacial Southern Ocean inferred from neodymium isotope ratios. Nature 405, 935–938.

Saenko, O.A., Schmittner, A., Weaver, A.J., 2004. The Atlantic-Pacific seesaw. J. Clim.

17, 2033–2038.
Sarnthein, M., Schneider, B., Grootes, P.M., 2013. Peak glacial ^{14}C ventilation ages suggest major draw-down of carbon into the abyssal ocean. Clim. Past. 9, 2595–2614.
Sarnthein, M., Winn, K., Jung, S.J., Duplessy, J.C., Labeyrie, L., Erlenkeuser, H., Ganssen, G., 1994. Changes in east Atlantic deepwater circulation over the last 30,000 years: Eight time slice reconstructions. Paleoceanography 9, 209–267.
Seidov, D., Maslin, M., 1999. North Atlantic deep water circulation collapse during Heinrich events. Geology 27, 23–26.
Shcherbina, A.Y., Talley, L.D., Rudnick, D.L., 2003. Direct observations of North Pacific ventilation: Brine rejection in the Okhotsk Sea. Science 302, 1952–1955.
Sherrell, R.M., Field, M.P., Ravizza, G., 1999. Uptake and fractionation of rare earth elements on hydrothermal plume particles at 9°45′N, East Pacific Rise. Geochim. Cosmochim. Acta 63, 1709–1722.
Siddall, M., Khatiwala, S., van de Flierdt, T., Jones, K., Goldstein, S.L., Hemming, S., Anderson, R.F., 2008. Towards explaining the Nd paradox using reversible scavenging in an ocean general circulation model. Earth Planet. Sci. Lett. 274, 448–461.
Soyol-Erdene, T.-O., Huh, Y., 2013. Rare earth element cycling in the pore waters of the Bering Sea Slope (IODP Exp. 323). Chem. Geol. 358, 75–89.
Springer, A.M., McRoy, C.P., Flint, M.V., 1996. The Bering Sea Green Belt: shelf-edge processes and ecosystem production. Fish. Oceanogr. 5, 205–223.
Stabeno, P.J., Kachel, N.B., Moore, S.E., Napp, J.M., Sigler, M., Yamaguchi, A., Zerbini, A.N., 2012. Comparison of warm and cold years on the southeastern Bering Sea shelf and some implications for the ecosystem. Deep-Sea Res. II 65, 31–45.
Stewart, J.A., Gutjahr, M., James, R.H., Anand, P., Wilson, P.A., 2016. Influence of the Amazon River on the Nd isotope composition of deep water in the western equatorial Atlantic during the Oligocene–Miocene transition. Earth Planet. Sci. Lett. 454, 132–141.
Stouffer, R.J., Yin, J., Gregory, J., Dixon, K., Spelman, M., Hurlin, W., Weaver, A., Eby, M., Flato, G., Hasumi, H., 2006. Investigating the causes of the response of the thermohaline circulation to past and future climate changes. J. Clim. 19, 1365–1387.
Tachikawa, K., Jeandel, C., Roy-Barman, M., 1999. A new approach to the Nd residence time in the ocean: the role of atmospheric inputs. Earth Planet. Sci. Lett. 170, 433–446.
Takahashi, K., Ravelo, A.C., Zarikian, C.A., 2011. IODP Expedition 323-Pliocene and Pleistocene paleoceanographic changes in the Bering Sea. Sci. Drill. 11, 4–13.
Talley, L.D., 1991. An Okhotsk Sea water anomaly: Implications for ventilation in the North Pacific. Deep-Sea Res. 38, S171–S190.
van de Flierdt, T., Frank, M., Lee, D.-C., Halliday, A.N., Reynolds, B.C., Hein, J.R., 2004. New constraints on the sources and behavior of neodymium and hafnium in seawater from Pacific Ocean ferromanganese crusts. Geochim. Cosmochim. Acta 68, 3827–3843.
van de Flierdt, T., Robinson, L.F., Adkins, J.F., 2010. Deep-sea coral aragonite as a recorder for the neodymium isotopic composition of seawater. Geochim. Cosmochim. Acta 74, 6014–6032.
VanLaningham, S., Pisias, N.G., Duncan, R.A., Clift, P.D., 2009. Glacial–interglacial sediment transport to the Meiji Drift, northwest Pacific Ocean: Evidence for timing of Beringian outwashing. Earth Planet. Sci. Lett. 277, 64–72.
von Blanckenburg, F., 1999. Tracing past ocean circulation? Science 286, 1862–1863.
Warner, M.J., Roden, G.I., 1995. Chlorofluorocarbon evidence for recent ventilation of the deep Bering Sea. Nature 373, 409–412.
Weis, D., Kieffer, B., Maerschalk, C., Pretorius, W., Barling, J., 2005. High-precision Pb-Sr-Nd-Hf isotopic characterization of USGS BHVO-1 and BHVO-2 reference materials. Geochem. Geophys. Geosyst. 6, Q02002 doi: 02010.01029/02004GC000852.
Wilson, D.J., Piotrowski, A.M., Galy, A., Clegg, J.A., 2013. Reactivity of neodymium carriers in deep sea sediments: Implications for boundary exchange and paleoceanography. Geochim. Cosmochim. Acta 109, 197–221.
Wilson, D.J., Piotrowski, A.M., Galy, A., McCave, I.N., 2012. A boundary exchange influence on deglacial neodymium isotope records from the deep western Indian Ocean. Earth Planet. Sci. Lett. 341–344, 35–47.
Yang, Y., Wu, F., Xie, L., Zhang, Y., 2009. High-precision measurements of the $^{143}Nd/^{144}Nd$ isotope ratio in certified reference materials without Nd and Sm separation by multiple collector inductively coupled plasma mass spectrometry. Anal. Lett. 43, 142–150.
Yasuda, I., 1997. The origin of the North Pacific Intermediate water. J. Geophys. Res. Oceans 102, 893–909 (1978-2012).